

Optical and transport properties of NbN thin films revisited

S. Kern,¹ P. Neilinger,^{1,2} M. Poláčková,¹ M. Baránek,¹ T. Plecenik,¹ T. Roch,¹ and M. Grajcar^{1,2}

¹*Department of Experimental Physics, Comenius University, SK-84248 Bratislava, Slovakia*

²*Institute of Physics, Slovak Academy of Sciences, Dúbravská cesta, Bratislava, Slovakia*

Highly disordered NbN thin films exhibit promising superconducting and optical properties. Despite extensive study, discrepancies in its basic electronic properties persist. Analysis of the optical conductivity of disordered ultra-thin NbN films, obtained from spectroscopic ellipsometry by standard Drude-Lorentz model, provides inconsistent parameters. We argue that this discrepancy arise from neglecting the presence of quantum corrections to conductivity in the IR range. To resolve this matter, we propose a modification to the Drude-Lorentz model, incorporating quantum corrections. The parameters obtained from the modified model are consistent not only with transport and superconducting measurements but also with ab initio calculations. The revisited values describing conduction electrons, which differ significantly from commonly adopted ones, are the electron relaxation rate $\Gamma \approx 1.8 \text{ eV}/\hbar$, the Fermi velocity $v_F \approx 0.7 \times 10^6 \text{ ms}^{-1}$ and the electron density of states $N(E_F) = 2 \text{ states of both spins/eV}/V_{\text{f.u.}}$.

I. INTRODUCTION

Niobium nitride (NbN) stands out for its excellent properties, including chemical stability, hardness, optical and superconducting characteristics.¹⁻⁴ Its relatively high superconducting critical temperature and large sheet resistance make it suitable for applications such as superconducting nanowire single photon detectors (SNSPDs)⁵ and kinetic inductance travelling wave parametric amplifiers (KITWPAs).⁶ Transition metal nitrides, including NbN, nowadays garner interest as plasmonic materials,⁷ exhibiting double epsilon-near-zero (ENZ) behaviour.⁸ This behaviour means that the real part of their dielectric function, $\epsilon_r(\omega)$, becomes zero at two frequencies below the UV range. ENZ materials enable strong interaction of light with plasma oscillations, offering a wide range of possibilities in photonics.⁹ NbN has drawn attention as an ENZ material due to its tunable plasma frequency through composition adjustments.¹⁰ Moreover, the optical response directly influences the efficiency of SNSPDs, emphasizing the importance of optical characterization of NbN thin films, as highlighted in Refs. 11.

Despite more than 50 years of extensive study of NbN films, significant disagreement persists with regards to some of their fundamental properties. The primary source of mismatch arises from seemingly contradictory results obtained through different measurement pathways.^{11,12} First, the characterisation of the disorder in NbN is routinely obtained from transport and Hall effect measurements. This is done via the Ioffe-Regel parameter $k_F l$, where k_F is the Fermi wavevector and l is the electron mean free path. It is well known that $k_F l$ close to unity can be obtained in thin NbN films, i.e. l is comparable to electron wavelength, and such highly disordered films are approaching metal-insulator transition (MIT).¹³⁻¹⁵ Alternatively, this criterion can be expressed via electron scattering rate in energy units $\hbar\Gamma$, which is comparable to the Fermi energy. Therefore, in highly disordered metals, $\hbar\Gamma$ is expected to be a couple eV. Sec-

ond, $\hbar\Gamma$ can be obtained from optical response as well, namely as a parameter of the Drude model for the dielectric function of conducting electrons. However, these measurements suggest $\hbar\Gamma \approx 0.33 \text{ eV}$ as obtained from fitting a Drude-Lorentz model to ellipsometric data in the visible range,^{11,16} which is an order of magnitude smaller than expected.

Thin NbN films, especially its δ -phase, have superior superconducting properties,¹⁷ and can be deposited by various methods,¹⁸⁻²⁰. They typically exhibit a polycrystalline structure with grains of various sizes, each possessing a relatively well-defined cubic lattice interrupted by vacancy defects.^{1,21} The grain boundaries consist of disordered NbN alloy, often containing oxygen, as well.^{22,23} Despite their granularity, NbN thin films can be considered as homogeneously disordered metal, especially regarding their optical response. This is natural in the case of high intergrain conductivity²⁴ or for mean free path that is small in comparison to the grain size.^{14,25}

It is known that the presence of disorder in metals, either granular or homogenous, leads to quantum corrections (QCs) to the Drude conductivity. In highly disordered metals, the density of states (DOS) at the Fermi level is suppressed, suppressing their conductivity, as well.²⁶ The correction to the real part of conductivity in 3D homogeneously disordered films, as obtained by Altshuler and Aronov in Ref. 26 as well as from scaling arguments,²⁷ can be expressed in the following unified form^{28,29}

$$\delta\sigma(\Omega) = -Q^2\sigma_0 \left(1 - \sqrt{\frac{\Omega}{\Gamma}} \right). \quad (1)$$

Here, σ_0 is the Drude conductivity, Q is the strength of the correction, also called quantumness.²⁸ The electron relaxation rate relates is defined as reciprocal relaxation time $\Gamma = 1/\tau$. The energy Ω is determined by various energy scales, such as incident photon energy $\hbar\omega$, temperature $\propto k_B T$, or magnetic field $\propto \mu_B B$. Although this behaviour is routinely observed at energies of the order of meV, it is rarely taken into account in optical

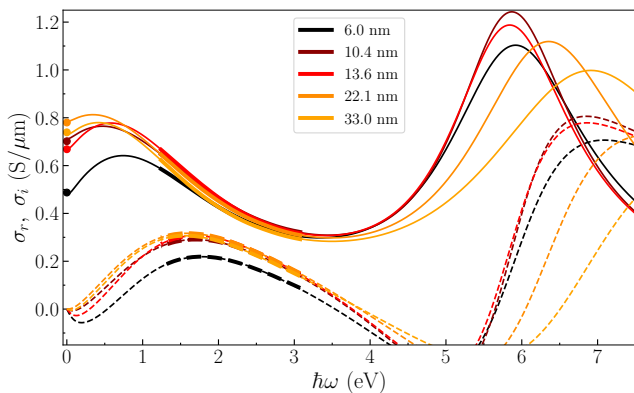


FIG. 1: Thick lines: real (solid) and imaginary (dashed) part of optical conductivity for NbN films of various thickness, determined by SE. Thin lines are fitted to Eq. (2). Circles: room-temperature DC conductivities measured by van der Pauw method.

response analysis.³⁰ Notably, in the study by Neilinger et al.,²⁸ the square root corrections (1) were observed up to optical frequencies in MoC thin films. Although not directly measured, a numerical study proposed a similar square root behavior in NbN.³¹

In the following, we argue that these corrections dramatically alter the optical properties of NbN films and explain the ENZ phenomenon. Modeling the optical conductivity by a quantum-corrected Drude-Lorentz model, we can determine various quantities, including the diffusion coefficient and the superconducting coherence length in agreement with the transport measurements. Moreover, the determined carrier density and agrees with the DFT. Additionally, we compare this model to commonly used models of the NbN dielectric function. The experimental data used to establish a consistent set of parameters, were obtained from spectroscopic ellipsometry (SE) on δ -NbN films of various thicknesses. Independent confirmation was provided by transport and magneto-resistance measurements.

II. OPTICAL PROPERTIES

The optical properties of NbN thin films were investigated utilizing SE in the range from 300 to 800 nm. Typically, SE is employed to determine the parameters (commonly layer thickness) of a chosen optical model for the studied sample. In our examination, where the goal is to select an appropriate optical model, we evaluate the optical constants directly from the SE data for each wavelength separately via a model-independent way (for details see Ref. 32).

The complex conductivity in the visible spectral range, determined from SE (thick lines in Fig. 1) is smooth and exhibits a clear dependence on the sample thickness. The real part of $\sigma(\omega)$ decreases with frequency for all samples

which is attributed to the Drude-like $1/\omega^2$ behaviour typical for metals with finite relaxation rate Γ .

In Ref. 31, a similar NbN film was studied, and a conductivity peak in the UV range was determined by means of numerical extrapolation. This spectral weight was attributed to inter-band transition at $\hbar\omega \approx 5-7$ eV. The presence of the inter-band transition, was observed through optical measurements^{10,33} and various ab-initio simulation, as well.^{10,34,35}

Furthermore, the numerical study presented in our previous work suggests that thin NbN films exhibit suppression of $\sigma_r(\omega)$ in the IR range, accompanied by a peak at ≈ 1 eV. This "anti-Drude" behaviour is also known as anomalous or displaced Drude peak. In Ref. 8, the peak in the optical conductivity of NbN films was explained in terms of an effective medium emerging from granular NbN dissolved in an insulating NbO matrix. We discuss this approach in Appendix A, where we argue that it is not appropriate for NbN, as it leads to unphysical conclusions.³⁶ In Ref. 36, the peak was obtained within the Drude-Smith model, which we analyze in Appendix B. In Ref. 30, the $\sigma_r(\omega)$ of metallic films close to MIT exhibited a square root dependence at frequencies below IR range, which was ascribed to quantum corrections to the Drude conductivity due to disorder. In order to describe the $\sigma_r(\omega)$ in the optical range, a "localization-modified Drude model" was suggested as a simple multiplication of the Drude formula with a square root term similar to Eq. (1).²⁹ However, this model leads to incorrect behaviour of the conductivity at high frequencies, which should drop as ω^{-2} . Moreover, this model poorly fits our data. The same square root behaviour of $\sigma_r(\omega)$ up to the visible range was observed in Ref. 28. But, it was suggested here that the influence of disorder should disappear at frequencies of the order of the relaxation rate. A square root correction was smoothly joined to the bare Drude conductivity at a crossover frequency, and an excellent agreement with the SE data was further confirmed by independent transmission measurements. Therefore, we analyse our SE data utilizing the quantum corrected Drude model, extended by a Lorentzian peak centred at ω_1 with strength σ_1 and width Γ_1 , describing the inter-band transition. The quantum correction exponentially vanishes at a scale $\Gamma/2$. Finally, we obtained following model for the complex conductivity

$$\sigma_r(\omega) = \frac{\sigma_0}{1 + (\omega/\Gamma)^2} \left(1 - \mathcal{Q}^2 (1 - \sqrt{\Omega/\Gamma}) e^{-\frac{1}{2}(\omega/r)^2} \right) + \frac{\sigma_1}{1 + \left(\frac{\omega_1^2 - \omega^2}{\omega\Gamma_1} \right)^2}, \quad (2)$$

$$\sigma_i(\omega) = \mathcal{H}[\sigma_r(\omega)] - (\epsilon_\infty - 1)\epsilon_0\omega. \quad (3)$$

To take into account the temperature smearing of the steep square root correction at low photon energies, following Ref. 28, an energy scale entering the correction was introduced as $\Omega = \sqrt{\omega^2 + (\pi k_B T/\hbar)^2}$. $\mathcal{H}[\sigma_r(\omega)]$

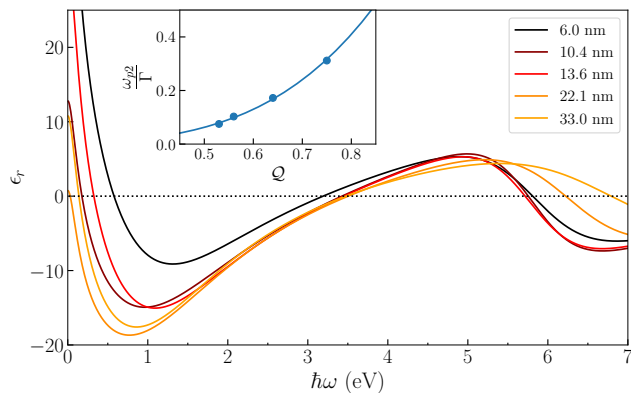


FIG. 2: The real part of the dielectric function $\epsilon(\omega)$ corresponding to the conductivities in Fig. 1. The inset shows the lower plasma frequencies (frequencies at which $\epsilon(\omega) = 0$) dependent on quantumness \mathcal{Q} . The solid line is a plot according to Eq. (5)

denotes the Hilbert transform of $\sigma_r(\omega)$, mathematically manifesting the Kramers-Kronig relations. The Hilbert transform can be performed numerically, or by approximative analytical formula for $\mathcal{H}[\sigma_r(\omega)]$, which we derived in Appendix C. This model of $\sigma_r(\omega)$ does not consider the inter-band transitions of bound electrons at high energies, which affects the imaginary conductivity even at small frequencies. Their effect is therefore expressed by the second term in Eq. (3) via the parameter $\epsilon_\infty = 1.6$ estimated in Appendix D.

In the Fig. 1, it is shown that the proposed model (thin lines) produces an excellent fit to both the real and the imaginary parts of the conductivity. The parameters of the best fit are listed in Table I. The Drude conductivity σ_0 and the parameters of the inter-band transition peak exhibit no clear dependence on thickness. On the contrary, the scattering rate Γ slightly increases with decreasing thickness, as expected. As Γ rises, \mathcal{Q} increases, too. This comes from the expression for \mathcal{Q} being $\approx 1/k_F l$, where $l = v_F/\Gamma$ and $v_F = \hbar k_F/m_e$ is the Fermi velocity, which we estimated as $v_F = \sqrt{\hbar\Gamma/(Qm_e)} \approx 0.7 - 0.8 \times 10^6 \text{ ms}^{-1}$.^{26,29}

The peak at 5-7 eV agrees with the predictions from the joint density of states calculation.³⁵ Similarly, the joint density of states calculation predicted transitions between the three highest occupied bands, leading to a peak in the dielectric function at approx. 1 eV. Therefore, it is tempting to assign the anomalous Drude peak to the inter-band transitions, as was done in Refs. 11,16. However, as can be seen from the angle-resolved photoemission spectroscopy (ARPES) measurement, the disorder and/or thickness-enhanced scattering smears the electron structure at the scale $\hbar\Gamma \approx 1.5 \text{ eV}$.³⁷ Furthermore, the DFT simulations suggest that such smearing is necessary to stabilize the crystalline structure of $\delta\text{-NbN}$.³⁸ Therefore, these inter-band transitions should not be present in the spectra. Also, modelling the dis-

placed Drude peak as an inter-band transition leads to a puzzling shift of its central frequency to higher energies with decreasing thickness, whereas for our model it is explained via the increase of the quantumness \mathcal{Q} .

The corresponding real part of the dielectric function (Fig. 2) given as $\epsilon_r(\omega) = 1 - \sigma_i(\omega)/\epsilon_0\omega$, exhibits the discussed double ENZ feature. For $\mathcal{Q} = 0$, the model gives (for $\epsilon_r(\omega)$ and for the ordinary screened plasma frequency ω_p) the well-known results

$$\epsilon_r(\omega) \approx \epsilon'_\infty - \frac{\sigma_0/\epsilon_0\Gamma}{(1 + (\omega/\Gamma)^2)} \rightarrow \omega_p^2 = \frac{\sigma_0\Gamma}{\epsilon_0\epsilon'_\infty}, \quad (4)$$

where $\epsilon'_\infty = \epsilon_\infty + \sigma_1\Gamma_1/(\epsilon_0\Omega_1^2)$ contains bound electrons contribution ϵ_∞ evaluated in Appendix D and the second term is contribution from the inter-band transition at $\approx 6 \text{ eV}$. From Eq. (C8), it can be shown, that for low energies $\hbar\omega$, the imaginary part is dominated by the square root term. This gives, for epsilon and for the newly unveiled second plasma frequency ω_{p2}

$$\epsilon_r(\omega) \approx \epsilon'_\infty - \frac{\sigma_0}{\epsilon_0\Gamma} \left(1 - \mathcal{Q}^2 \sqrt{\frac{\Gamma}{\omega}}\right) \rightarrow \quad (5)$$

$$\omega_{p2} \propto \Gamma\mathcal{Q}^4,$$

clearly showing that, for non-negligible \mathcal{Q} , the second, lower plasma frequency appears. Its value increases as \mathcal{Q}^4 , whereas the regular plasma frequency slightly decreases with \mathcal{Q} . In the inset of Fig. 2, the second plasma frequencies of the samples are plotted. The thickest sample with the lowest \mathcal{Q} does not reach zero, as the temperature smearing sufficiently suppresses the square root behaviour, which is not taken into account in Eq. (5).

d (nm)	σ_0 ($S\mu\text{m}^{-1}$)	$\hbar\Gamma$ (eV)	\mathcal{Q} (1)	σ_1 ($S\mu\text{m}^{-1}$)	$\hbar\Gamma_1$ (eV)	$\hbar\omega_1$ (eV)
6.0	0.88	1.86	0.75	0.72	2.38	5.64
10.4	0.94	1.89	0.56	0.77	2.04	5.51
13.6	1.01	1.80	0.64	0.81	1.80	5.36
22.1	0.95	1.84	0.45	0.77	2.23	5.74
33.0	0.95	1.73	0.53	0.68	3.10	6.20

TABLE I: Parameters of optical model (2) and (3) providing the best fit to the experimental data.

III. TRANSPORT AND SUPERCONDUCTING PROPERTIES

The introduced optical model, fitted to ellipsometric data, predicts the DC conductivity that was independently evaluated as $\sigma_{DC}(T = 300 \text{ K}) = 1/(R_\square d)$. Here, R_\square is the sheet resistance measured by the van der Pauw method at room temperature, and d is the thickness of

d (nm)	L (nm)	ρ (gcm^{-3})	R_{\square} (Ω)	RRR (1)	T_c (K)	$2k_B T_c$ (meV)
6.0	9	7.8	340	0.76	11.68	2.0
10.4	12	7.8	136	0.88	13.15	2.3
13.6	12	7.8	107	0.81	13.64	2.3
22.1	11	7.9	58	0.89	14.26	2.5
33.0	12	7.8	41	0.83	13.71	2.4

TABLE II: Properties of thin NbN obtained from X-ray measurements and temperature-dependent transport measurements. RRR is obtained as $R_{\square}/R_{\square}(20\text{ K})$, where R_{\square} is the room temperature sheet resistance.

the sample determined by the X-Ray reflection (XRR) measurements. Both values are listed in table II. The resulting DC conductivity is plotted in Fig. 1 as dots, and they are perfectly recovered by the low-frequency part of the optical conductivity fit. Here, we emphasize, that the DC conductivity was not utilized during the fitting procedure.

In literature, it is common to compute the electronic parameters (i.e. $k_F l$) from the measured DC conductivity $\sigma_{DC} = 1/(R_{\square} d)$, assuming it is equal to the Drude conductivity σ_0 . However, within our approach, the measured DC conductivity is $\sigma_{DC} = \sigma_0(1 - Q^2)$, therefore it can not be interchanged with the Drude conductivity σ_0 . Following Refs. 26,30, we equate the quantumness Q to $1/k_F l$, which enables us to easily estimate the Ioffe-Regel parameter as well as the diffusivity $D = v_F l/3 = \hbar k_F l/(3m_e) = \hbar/(3Qm_e)$.

To verify the diffusivity estimated from the optical measurements, the magneto-resistance at low temperatures was measured (see Fig. 3), and the temperature-dependence of the upper critical field $B_{c2}(T)$ was determined. We start with the Ginzburg-Landau (GL) result for the upper critical magnetic field

$$B_{c2} = \frac{\Phi_0}{2\pi\xi_{GL}^2(T)}, \quad (6)$$

where Φ_0 is the magnetic flux quantum and ξ_{GL} is the GL coherence length. In the dirty limit, $\xi_{GL}(T)$ satisfies

$$\frac{1}{\xi_{GL}^2(T)} = \frac{1}{0.855^2 \xi_0 l} \frac{T_c - T}{T_c}, \quad (7)$$

where $\xi_0 = \hbar v_F/(\pi\Delta)$ is the BCS coherence length, T_c is the superconducting critical temperature, and Δ is the superconducting gap. Recalling the BCS relation $\Delta = 1.764 k_B T_c$, one can express the diffusivity via the temperature derivative of B_{c2} as³⁹

$$D_{B_{c2}} = -\frac{4k_B}{\pi e} \left(\frac{\partial B_{c2}}{\partial T} \right)_{T_c}^{-1}. \quad (8)$$

The diffusivities were estimated from the slope of $B_{c2}(T)$ curves showed in Fig. 4. Comparison in the inset of

Fig. 4 shows that the diffusivity $D_{B_{c2}}$ estimated from the magneto-resistance is comparable to D_{opt} , calculated from the optical model. The expected decrease of the diffusivity at low thicknesses is present in D_{opt} , but $D_{B_{c2}}$ is increasing with lowering the film thickness. This paradoxical behaviour was likewise observed in Ref. 40. In Ref. 41 relation (8) was corrected to take into account that NbN is supposed to be a strong coupling superconductor. However, this would lead to further increase of $D_{B_{c2}}$. Alternatively, in Ref. 42 the authors showed that the broadened tunneling spectra of dirty superconductors, also known as Dynes superconductors, such as NbN^{43,44}, can be explained by the presence of two types of scattering processes, namely the pair-conserving and the pair-breaking scattering. The rate of these scatterings is Γ and Γ_D , respectively. They also calculated the thermodynamic properties of these superconductor, expressing the GL coherence length as⁴⁵

$$\frac{1}{\xi_{GL}^2(T)} = \frac{12[1 - \zeta(2, \frac{1}{2} + \alpha)]}{\pi\zeta(2, \frac{1}{2} + \alpha)} \frac{\hbar\Gamma}{\Delta} \frac{k_B(T_c - T)}{\Delta} \frac{1}{\xi_0^2}, \quad (9)$$

where $\alpha = \hbar\Gamma_D/(2\pi k_B T_c)$ and $\zeta(s, x)$ is the Hurwitz zeta function. Then, diffusivity can be expressed as

$$D'_{B_{c2}} = -K(\alpha) \frac{k_B}{e} \left(\frac{\partial B_{c2}}{\partial T} \right)_{T_c}^{-1}, \quad (10)$$

where $K = 2\pi[1 - \zeta(2, \frac{1}{2} + \alpha)]/\zeta(2, \frac{1}{2} + \alpha)$ and can be approximated by the expression

$$K(\alpha) \approx \frac{1.273 + 1.155\alpha}{1 + 2.432\alpha + 2.206\alpha^2}. \quad (11)$$

For $\alpha = 0$, the function $K(\alpha)$ reduces to the BCS value $4/\pi$, however, for thin films, α is non-zero and thus decreases the diffusivity. Comparing the diffusivity values $D_{B_{c2}}$ for the 6 nm sample and 30 nm samples, $\alpha = 0.15$ was estimated. This yields an estimate of $\hbar\Gamma_D = 0.9$ meV, which is reasonable for thin NbN films. $\hbar\Gamma_D$ estimated from tunneling spectra varies in the range from negligibly small values up to tenths of meV, and even as large as $\Delta/2$ for strongly disordered samples with suppressed T_c .^{17,43,46-49}

The electron mean free path was estimated as $l = \sqrt{\hbar/Q\Gamma m_e} \approx 2 - 3 \text{ \AA}$ is slightly above half of the lattice parameter $a = 4.4 \text{ \AA}$, which indicates that the samples are close to the Ioffe-Regel limit $k_F l \rightarrow 1$. The Ginzburg-Landau coherence length $\xi_{GL}(0)$ estimated by both Eqs. (7) and (9) ranges from 3 nm to 4 nm, which agrees with a commonly measured value in thin NbN films.^{41,50,51}

IV. DISCUSSION

It is now convenient to compare the revisited parameters of NbN with DFT simulations. We estimated the density of carriers in NbN as $n = \sigma_0 \Gamma m_e / e^2 = 9 \times 10^{28} \text{ m}^{-3} = 2 V_{f.u.}^{-1}$, where $V_{f.u.}$ is the formula unit

d	$k_F l$	D_{opt}	$D_{B_{c2}}$	l	v_F	ξ_0	ξ_{GL}	B_{c2}	$N(E_F)$	$E_F - E_c$	n
(nm)	(1)	(cm^2s^{-1})	(cm^2s^{-1})	(\AA)	(10^6ms^{-1})	(nm)	(nm)	(T)	($\text{eV}^{-1}V_{f.u.}^{-1}$)	(eV)	(10^{28}m^{-3})
	$1/Q$	$\frac{\hbar}{3Qm_e}$	$-\frac{4k_B}{\pi e} \left(\frac{\partial B_{c2}}{\partial T}\right)^{-1}_{T_c}$	$\sqrt{\frac{\hbar}{Q\Gamma m_e}}$	$\sqrt{\frac{\hbar\Gamma}{Qm_e}}$	$\frac{\hbar v_F}{\pi\Delta}$	$0.855\sqrt{\xi_{BCS}l}$	$\Phi_0/2\pi\xi_{GL}^2$	$\frac{3\sigma_0 Qm_e}{\hbar e^2}$	$\frac{\hbar\Gamma}{2Q}$	$\frac{\sigma_0\Gamma m_e}{e^2}$
6.0	1.33	0.51	0.73	2.34	0.66	69.2	3.44	27.0	2.27	1.24	8.82
10.4	1.78	0.69	0.68	2.68	0.77	70.2	3.71	23.1	1.81	1.69	9.57
13.6	1.56	0.60	0.60	2.57	0.70	64.1	3.47	26.5	2.23	1.41	9.80
22.1	2.22	0.86	0.63	3.03	0.85	71.1	3.97	20.2	1.47	2.04	9.42
33.0	1.88	0.73	0.57	2.88	0.76	66.1	3.73	22.9	1.73	1.63	8.86

TABLE III: Electronic properties calculated from the fit parameters of the proposed optical model to optical conductivity. For comparison, besides the calculated diffusivity D_{opt} , diffusivity $D_{B_{c2}}$ obtained from the temperature dependence of critical field $B_{c2}(T)$ is listed, too. For the BCS coherence length ξ_0 we used the estimate of superconducting gap from Table II: $\Delta \approx 2k_B T_c$.

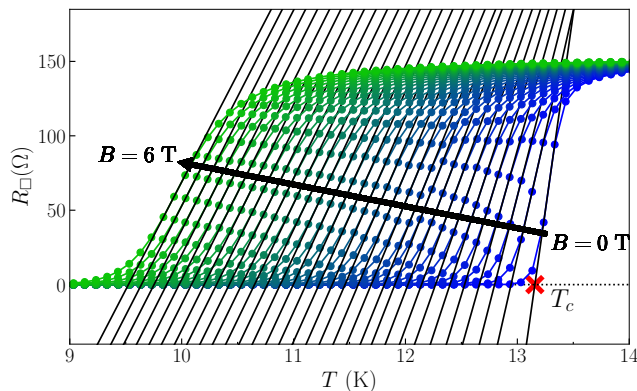


FIG. 3: Magnetic field variation of the temperature-dependent sheet resistance $R_{\square}(T)$ for the 10 nm sample. Black lines are given by the maximal slope of $R_{\square}(T)$ curves and the temperature of the superconducting transition is determined by the intersect of the maximal slope line (black solid lines) and the zero resistance line (black dotted line).

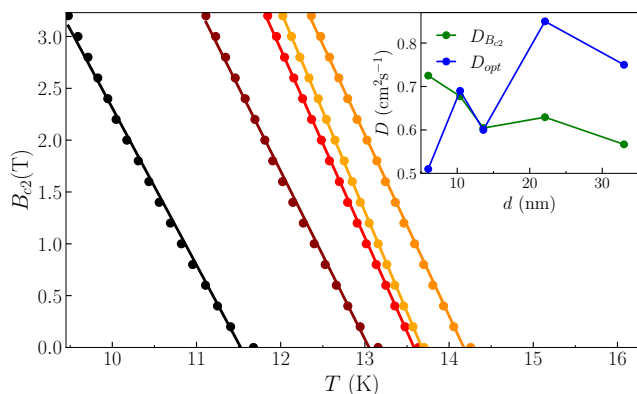


FIG. 4: Temperature dependence of the upper critical field B_{c2} . The solid lines are linear fits to the $B_{c2}(T)$ data. The color-coding is same as in Fig. 1. The inset shows a comparison of the diffusivity obtained from the slope of $B_{c2}(T)$ (green) and that estimated from the proposed optical model (blue).

volume, for δ -NbN $V_{f.u.} = a^3/4$. This result is in excellent agreement with the value obtained by integrating the DFT DOS from the threshold of the peak responsible for the modeled inter-band transition ($\approx E_F - 4$ eV) up to E_F .^{33,38,52-55} This also contradicts the common assumption, that all 4 Nb d-orbital electrons are conducting.¹⁷ We should emphasize here, that the agreement of our estimation of the number of electrons in the conductive band with the DFT result was obtained despite the fact that the DFT DOS itself is two times smaller than the "Drude" DOS, which we determined from the Einstein relation $N(E_F) = \sigma_0/(e^2 D_{opt})$. This can be explained by the fact that the determined bottom of the conductive band $E_c = E_F - 2$ eV is much closer to E_F compared to DFT result 4 eV. The value of $E_F - E_c$ was estimated from free electron relation between the density of electrons and DOS, given as $n = 2N(E_F)(E_F - E_c)/3$. Similar effect was observed in ARPES measurement where the conductive band was significantly flattened in comparison to the DFT calculation, naturally leading to higher DOS at the Fermi level.³⁷ The 1 eV scale of smearing of the ARPES bandstructure also suggest a high value of scattering rate Γ . Nevertheless, ARPES agrees with DFT on the value of the Fermi momentum being approximately half of the GL path with length $\sqrt{3}\pi/a = 1.24 \text{ \AA}^{-1}$. This agrees with the estimated $k_F \approx 0.6 \text{ \AA}^{-1}$.

For $N(E_F)$, we obtained 2 states of both spins/eV/ $V_{f.u.}$. Omitting the corrections, i.e., utilizing σ_{DC} instead of σ_0 , would lead to suppressed DOS $N' = (1 - Q^2)N(E_F)$ which is thickness-dependent.^{12,13} Here we point out that even though in Ref. 13 this suppressed DOS N' from transport measurements was successfully compared to DFT value, these are by nature different. Moreover, it should be noted that the DFT calculations only partially account for electron-electron or electron-phonon interactions, which are significant in NbN,⁵⁶. This implies that even the comparison of uncorrected Drude DOS $N(E_F)$ with the DFT value 0.8 - 1.2 states of both spins/eV/ $V_{f.u.}$ is questionable.

V. CONCLUSION

In conclusion, we argue that the quantum corrections to the conductivity of NbN films are present at optical frequencies and significantly alter their dielectric function. Therefore, we analyze their optical conductivities, utilizing the quantum-corrected Drude-Lorentz model. The proposed model yields to an excellent fit to the $\sigma(\omega)$ and provides parameters of the electronic fluid such as: the electron concentration n , the diffusion coefficient D , the Ioffe-Regel parameter $k_F l$, and the electronic density of states $N(E_F)$. The obtained diffusion coefficient agrees with the magneto-transport measurement, moreover, the estimated n is consistent with ab initio simulations. The determined electron relaxation rate $\hbar\Gamma \approx 1.8$ eV, consistent with the presence of high disorder in NbN films, is an order of magnitude higher than the commonly considered value obtained from standard optical models. This emphasizes the importance of quantum corrections in the analysis. Moreover, various puzzling phenomena like the double ENZ¹⁰, the increase of sheet resistance at lower thicknesses, and inconsistencies in electron relaxation rates are explained by this model. For other reported effects, such as increasing diffusivity with lowering of the thickness, and high electron density of states, we have suggested explanations, which could be verified by further experiments.

A. Acknowledgments

We thank to R. Hlubina and R. Martoňák for useful discussions. This work was supported by the Slovak Research and Development Agency under the contracts APVV-20-0425 and by the QuantERA grant SiUCs. M. Poláčková was supported by the Slovak Research and Development Agency under Contract No. APVV-19-0303.

It is also the result of support under the Operational Program Integrated Infrastructure for the projects: Advancing University Capacity and Competence in Research, Development and Innovation (ACCORD, ITMS2014+:313021X329) and UpScale of Comenius University Capacities and Competence in Research, Development and Innovation (USCCORD, ITMS 2014+:313021BUZ3), co-financed by the European Regional Development Fund.

Appendix A: Effective medium theory

In Ref. 8, the double ENZ was explained via Maxwell-Garnet (MG) effective medium theory, which describes the optical properties of composite materials consisting of polarizable inclusions in an insulating matrix. In the case of NbN, NbN nanoparticles are immersed in a matrix of insulating niobium oxides. Taking the dielectric function of the oxide from Ref. 57, the resulting MG formula provides $\epsilon(\omega)$ with two zeros. However, such effective

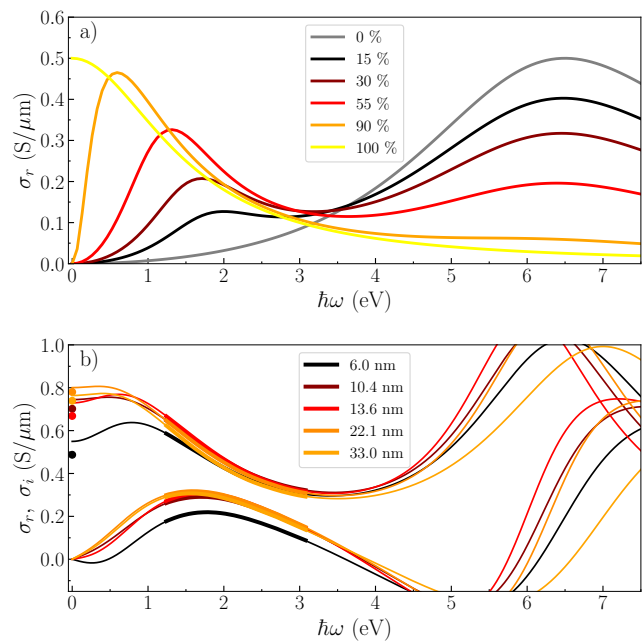


FIG. 5: a) Prediction of Maxwell-Garnet theory for a metallic inclusion in a niobium oxide matrix for various volume fractions of the inclusion. b) Thin lines are the Drude-Smith model curves obtained as best fit to data from ellipsometry depicted by thick lines. Points at zero frequency are the measured DC conductivities.

medium with an insulating matrix is inevitably an insulator. Moreover, the presence of oxygen in the NbN films was associated with the degree of porosity and it manifests itself in a significant increase of the resistance and/or the residual-resistance ration (RRR).²³ Considering the sheet resistance and RRR (see Table II), our samples have negligible oxygen content. The presence of oxygen should affect the density of the films as well,²³ which was estimated from XRR, to have a constant value of 7.8 gcm⁻³, which is close the ideal cubic NbN value.

If the matrix would be a bad conductor, with a conductivity peak at 5-7 eV, the MG model indeed reproduces both the suppression of the DC conductivity and the double ENZ behaviour. But, as can be seen in Fig. 5a, by varying the volume fraction of the inclusion, the model interpolates between the Drude conductivity and the conductivity of the poorly conducting matrix, i.e., the conductivity varies in the whole frequency range. Besides the DC conductivity suppression, $\sigma(\omega)$ would vary at energy $\approx \hbar\Gamma$, too, and the optical peak would change rapidly its weight. None of this behaviour was observed in the SE measurements.

Appendix B: Drude-Smith model

Another approach which yields to the anomalous Drude peak is the Drude-Smith model, which is based

d (nm)	σ_0 ($S\mu\text{m}^{-1}$)	$\hbar\Gamma_{\text{diff}}$ (eV)	c (1)	a (1)	σ_1 ($S\mu\text{m}^{-1}$)	$\hbar\Gamma_1$ (eV)	$\hbar\Omega_1$ (eV)
6.0	1.00	1.38	0.48	1.08	1.00	0.76	5.52
10.4	1.17	1.36	0.38	1.31	1.01	0.72	5.50
13.6	1.18	1.35	0.40	1.11	1.08	0.68	5.50
22.1	1.17	1.32	0.34	1.36	1.05	0.76	5.70
33.0	1.17	1.24	0.37	1.20	0.97	0.91	6.00

TABLE IV: Parameters of Drude-Smith model (B1) providing best fit to the experimental data.

on a material formed by granules whose boundaries cause reflection of electrons. This model, as derived in Ref. 36, leads to the following corrections to the Drude formula

$$\sigma(\omega) = \frac{\sigma_0}{1 - i\omega/\Gamma_{\text{diff}}} \left(1 - \frac{c}{1 - i\omega/a} \right). \quad (\text{B1})$$

Here, the parameters Γ_{diff} and a are determined by the granule size L , utilizing the following relations

$$\Gamma_{\text{diff}} = \frac{1}{\tau} + \frac{2v_{th}}{L}, \quad a = \frac{12v_{th}}{L} \frac{\tau}{L/v_{th} + 2\tau}, \quad (\text{B2})$$

where $v_{th} = \sqrt{k_B T/m_e}$ is the thermal velocity. This model fits our experimental data very well (see Fig. 5b). However, the resulting granule size is 5 Å, which is at least one order of magnitude smaller than the grain size estimated by X-Ray diffraction (XRD) measurement. For reasonable parameters (the measured grain size $L \approx 10$ nm and relaxation rate $1/\tau = \Gamma \approx 2$ eV/ \hbar), this model leads to a displaced Drude peak in THz frequency range (meV). Thus, the fit of this model to our data produces unreasonable parameters. We do not claim that this effect is not present as it still can play a role at much smaller energies, where our measurements are not sensitive.

Appendix C: Approximative formula for imaginary part of the modelled conductivity

The Drude-Lorentz and Drude-Smith models are convenient because both the real and the imaginary part are accessible in a simple closed formula. Therefore, they can be easily implemented in a fitting procedure, which are computationally less demanding. More complex models, typically expressing one part of the dielectric function, usually require to compute the other one numerically, as we have indeed done for the proposed model (2). However, we derived a simple approximative analytical formula for the KK image of $\sigma_r(\omega)$, too. We start by introducing the dimensionless frequency $x = \omega/\Gamma$ and expanding the exponential function

$$e^{-2x^2} = \left(1 + 2x^2 + \frac{1}{2}(2x^2)^2 + \dots \right)^{-1}. \quad (\text{C1})$$

Taking the first two terms, we obtained the approximative form of $\sigma_r(x)$

$$\tilde{\sigma}_r(x) = \frac{\sigma_0}{1+x^2} \left(1 - \mathcal{Q}^2 \frac{1-\sqrt{x}}{1+2x^2} \right). \quad (\text{C2})$$

Utilizing the fact that the real part of the conductivity is an even function of x , the Hilbert transform of Eq. (C2) is

$$\mathcal{H}[\sigma_r(x)] = \frac{2x}{\pi} \text{P.V.} \int_0^\infty \frac{\sigma_r(s)}{x^2 - s^2} dx. \quad (\text{C3})$$

For the imaginary part $\tilde{\sigma}_i(x)$ we obtained

$$\tilde{\sigma}_i(x) = \frac{\sigma_0 x}{1+x^2} \left(1 - \mathcal{Q}^2 \frac{ax^2 - b + 1/\sqrt{x}}{1+2x^2} \right), \quad (\text{C4})$$

where

$$\begin{aligned} a &= 2(2\sqrt{2} - 2^{3/4} - 1) \approx 0.293, \\ b &= (1 - 3\sqrt{2} + 2^{7/4}) \approx 0.121. \end{aligned} \quad (\text{C5})$$

The comparison of Eq. (C4) (red dashed lines) with the numerical result (green dashed lines) for various values of quantumness $\mathcal{Q} = 0, 0.5, 0.75, 1$ is in Fig. 6a. One can see a excellent match, except for the value $\mathcal{Q} = 1$, where a slight disagreement can be seen. This can be treated by taking the next term in the expansion (C1). We calculated the Hilbert transform of the function

$$\tilde{\sigma}_r(x) = \frac{\sigma_0}{1+x^2} \left(1 - \mathcal{Q}^2 \frac{1-\sqrt{x}}{1+2x^2+2x^4} \right), \quad (\text{C6})$$

with the result

$$\tilde{\sigma}_i(x) = \frac{\sigma_0 x}{1+x^2} \left(1 + \mathcal{Q}^2 \left(\sqrt{2} - \frac{(\alpha x^2 + \beta)(x^2 + 1) + 1 + 1/\sqrt{x}}{1+2x^2+2x^4} \right) \right), \quad (\text{C7})$$

where

$$\begin{aligned} \alpha &= 2 - 2^{7/4} \sin\left(\frac{\pi}{8}\right) + \frac{8}{\pi} \int_0^\infty \frac{x^{5/2} dx}{1+2x^2+2x^4} \approx 3.136, \\ \beta &= 2^{5/4} \sin\left(\frac{\pi}{8}\right) - \frac{4}{\pi} \int_0^\infty \frac{x^{1/2} dx}{1+2x^2+2x^4} \approx 0.308. \end{aligned} \quad (\text{C8})$$

In Fig. 6b we compare numerical transformations of Eq. (2) (green dashed lines) to the approximative formula (C6) (red dashed lines), indicating deviations smaller than 1 %. Finally, fitting the experimental data with the approximate formula for the imaginary part Eq. (C8) produces identical results as the numerical transformation does.

Appendix D: Electron structure and ϵ_∞ estimation

The picture of bonding and the configuration for 10 niobium and nitrogen valence electrons in NbN were proposed by many authors,^{54,56,58} and it was later largely

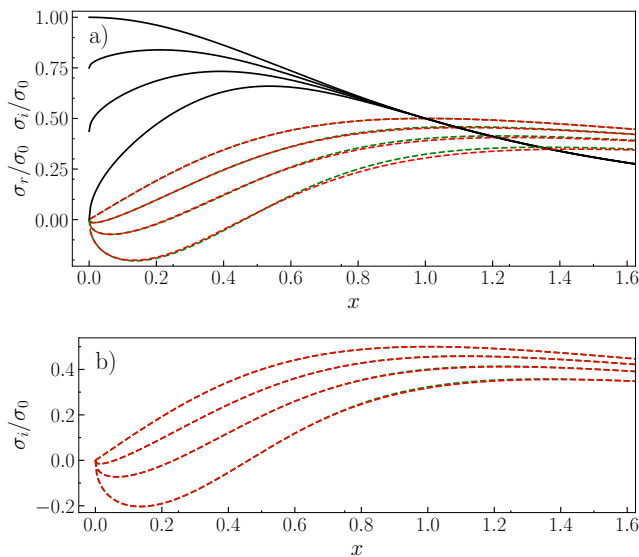


FIG. 6: a) Black lines are the modified Drude conductivity $\sigma_r(x)$ with quantum corrections of various strength $Q = 0, 0.5, 0.75, 1$. Green dashed lines are their corresponding Kramers-Kronig images obtained numerically. Red dashed lines are given by the formula (C4) for the Hilbert transforms of $\tilde{\sigma}_r(x)$. b) Green dashed lines are the same as in a), red dashed lines are plots of the formula (C6) for $\mathcal{H}[\tilde{\sigma}_r(x)]$.

confirmed by the partial DOS from DFT calculations and X-ray photoelectron spectroscopy.^{33,38} Namely, there is a complicated Fermi surface created by Nb's 4d orbitals occupied by two electrons.^{35,38} This agrees with the optical estimation of the Drude weight mentioned in the main text. Next, there is strong hybridization of Nb 4d and N 2p orbitals containing approx. 6 electrons forming a peak in DOS, approx. 6 eV below E_F , providing electrons for the modelled inter-band transition. A naive approach utilizing the strength and the width of the optical peak $Z = \sigma_1 \Gamma_1 m_e / (n_{NbN} e^2)$ gives 3-5 electrons. Here, $n_{NbN} = 1/V_{f.u.}$ is the concentration of formula units. The estimated number of electrons matches well with the band structure value, considering neglected joint DOS influence. Finally, the calculations indicate that the remaining 2 electrons occupy bands low in energy (10-20 eV below E_F), corresponding to N 2s orbitals. Contribution to the optical response due to the transition of these electrons to Fermi level is included via the parameter ϵ_∞ together with transitions of relevant remaining

core electrons.

Similarly to the estimation of the electron number in the DOS peak from the weight of the inter-band transition peak, we estimated the contribution ϵ_∞ to the dielectric function from high-energy transitions. In Ref. 28, the ϵ_∞ was expressed via the number of core electrons in their respective atomic level k , i.e. Z_k , as follows

$$\epsilon_\infty \approx 1 + \sum_k \frac{Z_k \Omega_k^2}{\omega_k^2}, \quad \Omega_k^2 = \frac{n_{NbN} e^2}{m_e \epsilon_0}. \quad (D1)$$

Here $\hbar\omega_k$ is the energy of the atomic level k with respect to the Fermi level. The values of $\hbar\omega_k$ are listed in Ref. 59. The relevant orbitals which are not too low in energy for niobium are $3s^2$, $3p^6$, $3d^{10}$, and $4s^2$, with energies 467 eV, 370 eV, 203 eV, and 56 eV, respectively. Nitrogen contributes with $1s^2$ and $2s^2$, with energies 410 eV and 37 eV, respectively. The energy of the nitrogen's 2s orbital is not taken from Ref. 59, but instead, the value 15 eV was taken, which is suggested by the predictions on the NbN electronic band structure, summarized in the previous paragraph. Finally, we obtained $\epsilon_\infty = 1.62$.

Appendix E: Sample preparation

The thin NbN films were prepared by pulsed laser deposition (PLD, Omicron system with Coherent Compex Pro 201 F laser) by means of a KrF laser with wavelength of 248 nm and pulse duration of 35 ns. The films were grown on c-cut sapphire substrates cleaned in ultrasonic bath in acetone, isopropyl alcohol, and deionized water in succession. The deposition was performed in high-vacuum chamber with the residual atmosphere pressure of 10^{-7} Pa. The ablation was carried out from a niobium target in $N_2 + 1\%H_2$ reactive atmosphere. The pressure of the atmosphere was 9.3 Pa and the substrate was heated up to 600°C. For more details see Ref. 19.

¹ L. Toth, *Transition metal carbides and nitrides* (Elsevier, 2014).

² A. Pogrebnjak, V. Rogoz, O. Bondar, N. Erdybaeva, and S. V. Plotnikov, *Protection of Metals and Physical Chemistry of Surfaces* **52**, 802 (2016).

³ A. Banerjee, R. M. Heath, D. Morozov, D. Hemakumara, U. Nasti, I. Thayne, and R. H. Hadfield, *Optical Materials*

Express **8**, 2072 (2018).

⁴ D. Hazra, N. Tsavdaris, S. Jebari, A. Grimm, F. Blanchet, F. Mercier, E. Blanquet, C. Chapelier, and M. Hofheinz, *Superconductor Science and Technology* **29**, 105011 (2016).

⁵ G. Gol'Tsman, O. Okunev, G. Chulkova, A. Lipatov, A. Semenov, K. Smirnov, B. Voronov, A. Dzardanov,

- C. Williams, and R. Sobolewski, Applied physics letters **79**, 705 (2001).
- 6 A. Adamyan, S. De Graaf, S. Kubatkin, and A. Danilov, Journal of Applied Physics **119** (2016).
 - 7 P. Karl, M. Ubl, M. Hentschel, P. Flad, Z.-Y. Chiao, J.-W. Yang, Y.-J. Lu, and H. Giessen, Optical Materials Express **10**, 2597 (2020).
 - 8 R. Bower, M. P. Wells, F. Johnson, R. Kilmurray, B. Doiron, E. Cali, G. Mallia, B. Zou, A. P. Mihai, N. M. Harrison, et al., Applied Surface Science **569**, 150912 (2021).
 - 9 J. Wu, Z. T. Xie, Y. Sha, H. Fu, and Q. Li, Photonics Research **9**, 1616 (2021).
 - 10 Y. Ran, H. Lu, S. Zhao, Q. Guo, C. Gao, Z. Jiang, and Z. Wang, Applied Surface Science **537**, 147981 (2021).
 - 11 A. Semenov, B. Günther, U. Böttger, H.-W. Hübers, H. Bartolf, A. Engel, A. Schilling, K. Ilin, M. Siegel, R. Schneider, et al., Physical Review B **80**, 054510 (2009).
 - 12 M. Sidorova, A. Semenov, H.-W. Hübers, K. Ilin, M. Siegel, I. Charaev, M. Moshkova, N. Kaurova, G. N. Goltsman, X. Zhang, et al., Physical Review B **102**, 054501 (2020).
 - 13 S. Chockalingam, M. Chand, J. Jesudasan, V. Tripathi, and P. Raychaudhuri, Physical Review B **77**, 214503 (2008).
 - 14 Y. Pellán, G. Dousselin, J. Pinel, and Y. Sohn, Journal of Low Temperature Physics **78**, 63 (1990).
 - 15 M. Chand, G. Saraswat, A. Kamlapure, M. Mondal, S. Kumar, J. Jesudasan, V. Bagwe, L. Benfatto, V. Tripathi, and P. Raychaudhuri, Physical Review B **85**, 014508 (2012).
 - 16 N. Kuz'michev and G. Motulevich, ZhETF **84**, 2316 (1983).
 - 17 M. Chand, Ph.D. thesis, Citeseer (2012).
 - 18 A. Kafizas, C. J. Carmalt, and I. P. Parkin, Coordination Chemistry Reviews **257**, 2073 (2013).
 - 19 S. Volkov, M. Gregor, T. Roch, L. Satrapinsky, B. Grančič, T. Fiantok, and A. Plecenik, Journal of Electrical Engineering **70**, 89 (2019).
 - 20 M. Ziegler, L. Fritzsche, J. Day, S. Linzen, S. Anders, J. Toussaint, and H.-G. Meyer, Superconductor Science and Technology **26**, 025008 (2012).
 - 21 S.-Z. Lin, O. Ayala-Valenzuela, R. D. McDonald, L. N. Bulaevskii, T. G. Holesinger, F. Ronning, N. R. Weisse-Bernstein, T. L. Williamson, A. H. Mueller, M. A. Hoffbauer, et al., Physical Review B **87**, 184507 (2013).
 - 22 W. Lengauer and P. Ettmayer, Monatshefte für Chemie/Chemical Monthly **117**, 275 (1986).
 - 23 R. Cabanel, J. Chaussy, J. Geneste, J. Mazuer, and J. Villegier, Thin solid films **185**, 145 (1990).
 - 24 I. Beloborodov, A. Lopatin, V. Vinokur, and K. B. Efetov, Reviews of Modern Physics **79**, 469 (2007).
 - 25 G. Reiss, J. Vancea, and H. Hoffmann, Physical review letters **56**, 2100 (1986).
 - 26 B. Altshuler and A. Aronov, in *Electron-Electron Interactions in Disordered Systems*, edited by A. Efros and M. Pollak (North Holland, 1985).
 - 27 W. McMillan, Physical Review B **24**, 2739 (1981).
 - 28 P. Neilinger, J. Greguš, D. Manca, B. Grančič, M. Kopčík, P. Szabó, P. Samuely, R. Hlubina, and M. Grajcar, Physical Review B **100**, 241106 (2019).
 - 29 M. Kaveh and N. Mott, Journal of Physics C: Solid State Physics **15**, L707 (1982).
 - 30 K. Lee, R. Menon, C. Yoon, and A. Heeger, Physical Review B **52**, 4779 (1995).
 - 31 S. Kern, P. Neilinger, D. Manca, J. Greguš, S. Volkov, and M. Grajcar, Physical Review B **103**, 134205 (2021).
 - 32 P. Neilinger, S. Kern, D. Manca, and M. Grajcar, in *AIP Conference Proceedings* (AIP Publishing, 2021), vol. 2411.
 - 33 R. Sanjinés, M. Benkahoul, C. Sandu, P. Schmid, and F. Lévy, Thin Solid Films **494**, 190 (2006).
 - 34 C. Fong and M. L. Cohen, Physical Review B **6**, 3633 (1972).
 - 35 J. Pflüger, J. Fink, W. Weber, K.-P. Bohnen, and G. Crececius, Physical Review B **31**, 1244 (1985).
 - 36 T. L. Cocker, D. Baillie, M. Buruma, L. V. Titova, R. D. Sydora, F. Marsiglio, and F. A. Hegmann, Physical Review B **96**, 205439 (2017).
 - 37 T. Yu, J. Wright, G. Khalsa, B. Pamuk, C. S. Chang, Y. Matveyev, X. Wang, T. Schmitt, D. Feng, D. A. Muller, et al., Science Advances **7**, eabi5833 (2021).
 - 38 K. R. Babu and G.-Y. Guo, Physical Review B **99**, 104508 (2019).
 - 39 H. Bartolf, in *Fluctuation Mechanisms in Superconductors: Nanowire Single-Photon Counters, Enabled by Effective Top-Down Manufacturing* (Springer, 2015), pp. 181–184.
 - 40 S. Ezaki, K. Makise, B. Shinozaki, T. Odo, T. Asano, H. Terai, T. Yamashita, S. Miki, and Z. Wang, Journal of Physics: Condensed Matter **24**, 475702 (2012).
 - 41 A. Shoji, S. Kiryu, and S. Kohjiro, Applied physics letters **60**, 1624 (1992).
 - 42 F. Herman and R. Hlubina, Physical Review B **94**, 144508 (2016).
 - 43 Y. Noat, V. Cherkez, C. Brun, T. Cren, C. Carbillet, F. Debontridder, K. Ilin, M. Siegel, A. Semenov, H.-W. Hübers, et al., Physical Review B **88**, 014503 (2013).
 - 44 S. Chaudhuri, M. Nevala, and I. Maasilta, Applied Physics Letters **102** (2013).
 - 45 F. Herman and R. Hlubina, Physical Review B **97**, 014517 (2018).
 - 46 M. Šindler, R. Tesař, J. Koláček, P. Szabó, P. Samuely, V. Hašková, C. Kadlec, F. Kadlec, and P. Kužel, Superconductor Science and Technology **27**, 055009 (2014).
 - 47 D. Henrich, *Influence of material and geometry on the performance of superconducting nanowire single-photon detectors*, vol. 10 (KIT Scientific Publishing, 2014).
 - 48 C. Carbillet, V. Cherkez, M. Skvortsov, M. Feigel'man, F. Debontridder, L. Ioffe, V. Stolyarov, K. Ilin, M. Siegel, D. Roditchev, et al., Physical Review B **102**, 024504 (2020).
 - 49 A. Kamlapure, T. Das, S. C. Ganguli, J. B. Parmar, S. Bhattacharyya, and P. Raychaudhuri, Scientific reports **3**, 2979 (2013).
 - 50 A. Engel, A. Semenov, H.-W. Hübers, K. Il'in, and M. Siegel, New Frontiers in Superconductivity Research **6**, 153 (2006).
 - 51 J. Jesudasan, M. Mondal, M. Chand, A. Kamlapure, S. Kumar, G. Saraswat, V. C. Bagwe, V. Tripathi, and P. Raychaudhuri, in *AIP Conference Proceedings* (American Institute of Physics, 2011), vol. 1349, pp. 923–924.
 - 52 T. Amriou, B. Bouhafs, H. Aourag, B. Khelifa, S. Bresson, and C. Mathieu, Physica B: Condensed Matter **325**, 46 (2003).
 - 53 D. Papaconstantopoulos, W. Pickett, B. Klein, and L. Boyer, Physical Review B **31**, 752 (1985).
 - 54 K. Schwarz, Journal of Physics C: Solid State Physics **10**, 195 (1977).
 - 55 B. Palanivel, G. Kalpana, and M. Rajagopalan, physica status solidi (b) **176**, 195 (1993).
 - 56 T. Geballe, B. Matthias, J. Remeika, A. Clogston, V. Compton, J. Maita, and H. Williams, Physics Physique

- Fizika **2**, 293 (1966).
- ⁵⁷ A. O'Hara, T. N. Nunley, A. B. Posadas, S. Zollner, and A. A. Demkov, *Journal of Applied Physics* **116** (2014).
- ⁵⁸ K. Schwarz, *CRC Crit. Rev. Solid State Mater. Sci.:(United States)* **13** (1987).
- ⁵⁹ *Electron binding energies, in electron volts, for the elements in their natural forms*, https://xdb.lbl.gov/Section1/Table_1-1.pdf, accessed: 2024-01-26.